Spin Jahn-Teller antiferromagnetism in $CoTi_2O_5$

Franziska K. K. Kirschner,[1,*] Roger D. Johnson,[1] Franz Lang,[1] Dmitry D. Khalyavin,[2] Pascal Manuel,[2] Tom Lancaster,[3] Dharmalingam Prabhakaran,[1] and Stephen J. Blundell[1,†]

[1] *Department of Physics, University of Oxford, Clarendon Laboratory, Parks Road, Oxford, OX1 3PU, United Kingdom*

[2] *ISIS Facility, Rutherford Appleton Laboratory, Harwell Oxford, Didcot OX11 0QX, United Kingdom*

[3] *Centre for Materials Physics, Durham University, Durham DH1 3LE, United Kingdom*

(Dated: November 24, 2018)

We have used neutron powder diffraction to solve the magnetic structure of orthorhombic $CoTi_2O_5$, showing that the long-range ordered state below 26 K identified in our muon-spin rotation experiments is antiferromagnetic with propagation vector $\mathbf{k} = (\pm\frac{1}{2}, \frac{1}{2}, 0)$ and moment of $2.72(1)\mu_B$ per Co^{2+} ion. This long range magnetic order is incompatible with the experimentally determined crystal structure because the imposed symmetry completely frustrates the exchange coupling. We conclude that the magnetic transition must therefore be accompanied by a spin Jahn-Teller effect which lowers the structural symmetry and thereby relieves the frustration. These results show that $CoTi_2O_5$ is a highly unusual low-symmetry material exhibiting a purely spin-driven lattice distortion critical to the establishment of an ordered magnetic ground state.

I. INTRODUCTION

The Jahn-Teller effect is the spontaneous lowering of symmetry that lifts an orbital degeneracy[1] and involves a coupling of the orbital and lattice degrees of freedom. In some rather rare cases an analogous effect can occur in which spin, rather than orbital, degrees of freedom play a role. This *spin Jahn-Teller effect* has been identified in pyrochlores in which the large spin degeneracy in the lattice of corner-sharing tetrahedra can be relieved by a distortion in those tetrahedra.[2,3] In some cubic spinels an analogous effect can take place in which a tetragonal distortion relieves the frustration.[4,5] A related effect has also been observed near level-crossing in molecular wheels.[6,7] In this paper we demonstrate the existence of spin Jahn-Teller driven antiferromagnetism in $CoTi_2O_5$, a compound which has much lower symmetry than either pyrochlores or spinels, showing that spin-phonon coupling can induce order in a larger class of materials than has previously been appreciated. The site symmetry of the magnetic Co^{2+} ($3d^7$) ion is $m2m$ (C_{2v}) and so the orbital levels are already non-degenerate (so no longer susceptible to a conventional Jahn-Teller transition). Nevertheless, we show that long range spin order is only permitted in the presence of the structural distortion that we predict to set in at $T_N = 26$ K.

Cobalt titanates are of interest due to their numerous applications. Co_2TiO_4 has a complex spinel magnetic structure,[8–11] which has found uses in catalysis,[12,13] microwave devices,[14] and Li-ion cells.[15] $CoTiO_3$ has been used as a photocatalyst,[16] gas sensor,[17] and also in semiconductor transistors and memory storage.[18] $CoTi_2O_5$, however, is less well-studied. It is the only cobalt titanate to melt incongruently,[19] and its pseudo-brookite structure[20] is an entropy-stabilized high temperature phase[21] which is susceptible to decomposition below 1414 K.[22,23] Only recently has it become possible to synthesize high-quality single crystals of $CoTi_2O_5$.[24]

II. EXPERIMENTAL DETAILS

A polycrystalline $CoTi_2O_5$ powder sample was prepared using high purity (> 99.99%) Co_3O_4 and TiO_2 via the solid state reaction technique. Mixed powders were sintered at 1200 °C for 48h in air with intermediate grinding. After confirming the phase purity of the powder using x-ray diffraction, a cylindrical rod of diameter 10 mm and length 100 mm was sintered at 1250 °C in air for 12 h. Finally, the single crystal was grown in a four-mirror optical floating-zone furnace (Crystal System Inc.) in argon/oxygen mixed gas (90:10 ratio) atmosphere with a growth rate of 2–3mm/h.

Neutron powder diffraction (NPD) measurements were performed on the WISH time-of-flight diffractometer[25] at ISIS, the UK Neutron and Muon Source. A highly pure, single crystal sample was ground to a fine powder (mass ∼1 g) and loaded into a cylindrical vanadium can, which was mounted within a ^{4}He cryostat. Data were collected with high counting statistics at 1.5 K, deep into the long-range ordered magnetic phase, and at 100 K in the paramagnetic phase. Data with lower counting statistics were also collected as a function of temperature throughout the magnetically ordered phase. All diffraction data were refined using FULLPROF.[26] High resolution x-ray powder diffraction data were collected from the same sample using a PANalytical Xpert powder diffractometer at 12 K using an Oxford Cryosystems Pynix closed-cycle refrigerator.

The magnetic susceptibility measurements were made using a Quantum Design MPMS, while the heat capacity measurements were made using a Quantum Design PPMS. Zero field μSR (ZF-μSR) experiments[27,28] were performed on a 0.2 g single crystal using a Quantum Continuous Flow Cryostat mounted on the general purpose spectrometer (GPS) at the Swiss Muon Source (spin rotator at ∼45° to the muon momentum). All of the μSR data were analyzed using WiMDA.[29]

Atom	Wyckoff position	x	y	z	$U_{\rm iso}$
Co	4c	0	0.1911(6)	1/4	0.012(3)
Ti	8f	0	0.1336(3)	0.5677(3)	0.013(1)
O1	4c	0	0.7853(2)	1/4	0.018(1)
O2	8f	0	0.0461(2)	0.1129(1)	0.0155(8)
O3	8f	0	0.3149(2)	0.0596(1)	0.0168(8)

TABLE I. Crystallographic parameters for $CoTi_2O_5$ refined against neutron powder diffraction data collected at 100 K. Cation order between Co and Ti sites, assuming a stoichiometric composition, was refined to 97.2(4)%. The measured lattice parameters are $a = 3.72649(8)$ Å, $b = 9.7005(2)$ Å, and $c = 10.0731(2)$ Å. The reliability parameters are $R_{\rm Bragg} = 3.21\%$, $R = 4.03\%$, and $wR = 3.10\,\%$.

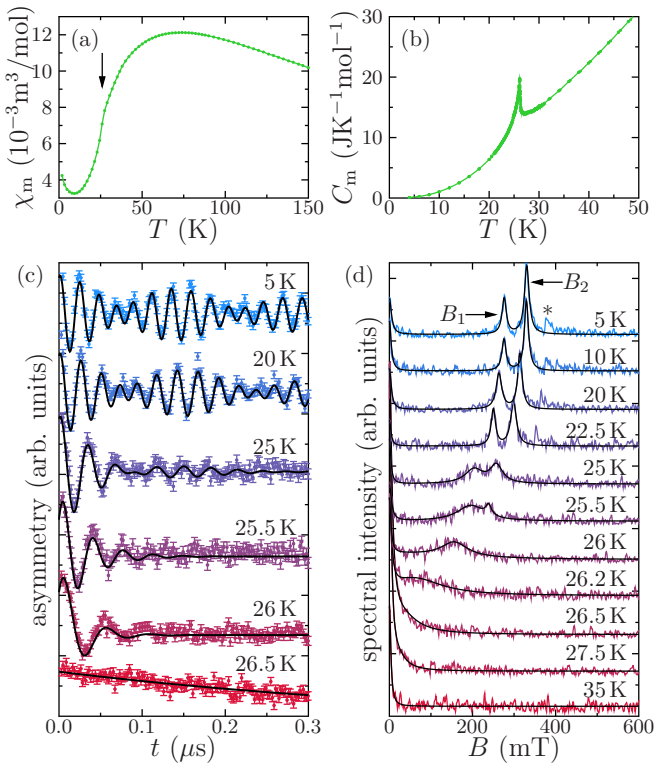

FIG. 1. (a) Magnetic susceptibility of $CoTi_2O_5$ measured in an applied field of $\mu_0 H = 0.1$ mT. The asterisk marks a kink at $T_{\rm N}$. (b) Molar heat capacity. (c) ZF-μSR spectra above and below $T_{\rm N}$. Fits to Eq. A1 are also plotted. (d) The Fourier transform of these spectra with fits with Eq. 1. The asterisk indicates an additional feature, discussed in the main text.

III. RESULTS

A. Magnetic susceptibility and heat capacity

Magnetic susceptibility and heat capacity data are shown in Fig. 1(a) and (b) respectively and are consistent with a magnetic transition at 26 K. The calculated entropy associated with the transition is 48% of the expected $R\ln(4)$ associated with the spin-only moment, indicative of significant correlations above $T_{\rm N}$.

B. Muon spin rotation

ZF-μSR asymmetry spectra $A(t)$ are shown in Fig. 1(c). At low T, we observe an oscillatory beating pattern of $A(t)$, along with two peaks in the Fourier transform spectra [Fig. 1(d)]. This is indicative of long-range magnetic order and two magnetically inequivalent muon stopping sites. The data can be fitted either in the time domain (see Appendix A) or in the field domain.

Below $T_{\rm N}$, the spectral intensity $I(B)$ in the field domain can be modelled with a sum of three Lorentzian distributions:

$$I(B) = I_1 L(B; B_1, \lambda_1) + I_2 L(B; B_2, \lambda_2) + I_{\rm b} L(B; 0, \lambda_{\rm b}), \quad (1)$$

where $L(B; B_i, \lambda_i)$ is a Lorentzian distribution centred on B_i with a width λ_i/γ_μ ($\gamma_\mu = 2\pi \times 135.5\,{\rm MHzT}^{-1}$ is the gyromagnetic ratio of the muon). The first two terms correspond to muons precessing in the internal fields of the sample; the two frequencies correspond to the two different fields at symmetry-inequivalent muon stopping sites. The Lorentzian distribution associated with each precession frequency indicates a small spread in the magnetic field distribution at the muon site, possibly due to the site disorder that has been observed between the Co and Ti sites in $CoTi_2O_5$ (as reported in Ref. 20 and refined as described below), small fluctuations of the Co moments, or due to muons near the boundaries of magnetic domains. The third term is a background term, corresponding to muons which land in the cryostat and sample holder, and therefore do not experience any of the sample's internal fields [the small width of this component, $\lambda_{\rm b} \approx 4$ mT for all T, may be due to these muons experiencing a small field close to the surface of the sample]. The fraction of muons contributing to each peak in Fig. 1(d) f_i is given by the area under that peak. The total fraction of muons experiencing a non-zero field, $f_B = (f_1 + f_2)/(f_1 + f_2 + f_3)$, is plotted in Fig. 2(a). The drop in f_B above $T_{\rm N}$ marks the transition into the paramagnetic state. (Similar conclusions can be obtained by fitting the data in the time domain as shown in Appendix A.)

The fitted values from Eq. 1 for the T evolution of λ_i and B_i are presented in Figs. 2(b) and (c) respectively. As T increases towards $T_{\rm N}$, the two peaks broaden and merge, while their centers move towards 0 T as the long-range-ordered magnet undergoes a transition to the paramagnetic regime. The data in Fig. 2(c) were fitted with the phenomenological formula $B = B_0\,(1 - (T/T_{\rm N})^\alpha)^\beta$, giving $T_{\rm N} = 26.0(11)$ K for both components. We also find values of the internal fields at the muon sites as $T \to 0$: $B_1 = 330(3)$ mT and $B_2 = 276(6)$ mT. There appears to be an additional small feature in the data at low T at ≈ 400 mT [marked by the asterisk in Fig. 1(d)], which

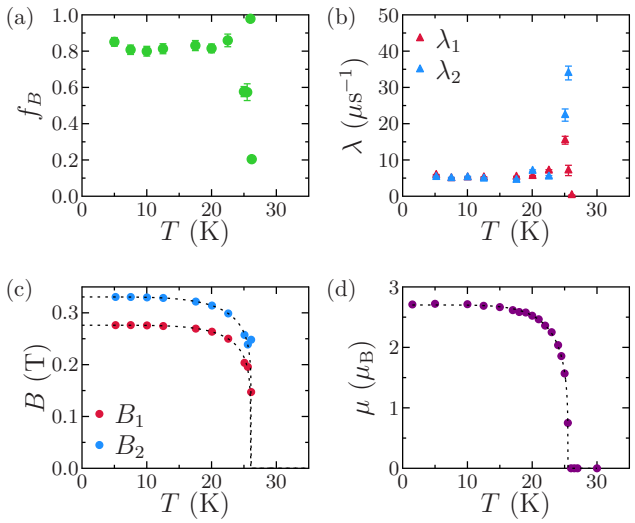

FIG. 2. (a) Temperature dependence of the fraction of muons experiencing a coherent magnetic field. Temperature dependences of the peak width and centers, as fitted from Eq. 1 applied to the Fourier transform of the ZF-μSR spectra, are shown in (b) and (c) respectively. (d) Temperature dependence of the Co magnetic moment extracted from neutron data. The dotted lines in (c) and (d) show phenomenological fits.

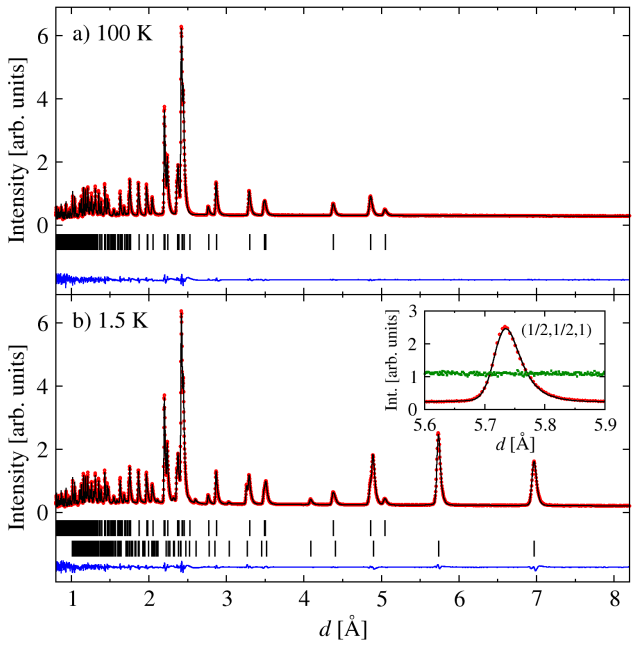

FIG. 3. Neutron powder diffraction data (red points) measured in bank 2 (average $2\theta = 58.3°$) of the WISH diffractometer from $CoTi_2O_5$ in (a) the paramagnetic phase and (b) the antiferromagnetic phase. The fitted *Cmcm* nuclear model (a) and nuclear + magnetic model (b), as described in the text, are shown as solid black lines. The respective peak positions are shown as black tick marks (nuclear top, magnetic bottom). Difference patterns ($I_{\rm obs} - I_{\rm calc}$) are given as solid blue lines at the bottom of the panels. The inset shows a blow-up of the 1.5 K data near the $(\frac{1}{2}, \frac{1}{2}, 1)$ peak (red points) together with low-temperature x-ray data in the same region (green points), demonstrating that the neutron peak is magnetic.

may arise due to the site disorder (see Appendix A).

C. Neutron powder diffraction

NPD data collected at 100 K (well above $T_{\rm N}$) were fitted with a nuclear model based upon the published crystal structure.[20] The goodness-of-fit was excellent, the data and fit are shown in Fig. 3(a), and the refined structural parameters are given in Table I. There was no evidence of impurity phases in these data. There is a small amount of site mixing whereby 2.8% of Co sites are occupied by Ti, and 1.4% of Ti sites are occupied by Co.

When compared to the NPD pattern at 100 K, data collected at 1.5 K showed more than 10 new diffraction peaks (Fig. 3(b)). Based on measurements of bulk properties and the results of our ZF-μSR experiments, we could robustly assign the origin of the new intensities to long-range magnetic order; furthermore, these new peaks are absent from our low-temperature x-ray data [see inset to Fig. 3(b)] and follow a typical q-dependence for a magnetic form factor, again demonstrating their magnetic origin. The observation of such a large number of magnetic diffraction peaks allowed us to unambiguously determine the magnetic propagation vector, which was found to be $\mathbf{k}_1 = (\frac{1}{2}, \frac{1}{2}, 0)$, or $\mathbf{k}_2 = (-\frac{1}{2}, \frac{1}{2}, 0)$, or both. Note that these two vectors are distinct, i.e. they are not related by an allowed reciprocal lattice vector of the C-centred parent structure, yet they cannot be distinguished by powder diffraction.

D. Symmetry analysis and magnetic structure

Symmetry analysis was performed using the ISOTROPY Suite [4,5], taking the *Cmcm* crystal structure of $CoTi_2O_5$[20] as the parent. Four irreducible representations enter into the decomposition of the magnetic reducible representation of $\mathbf{k}_1$ and $\mathbf{k}_2$ for the relevant Co Wyckoff positions. Through systematic tests it was found that the magnetic structures of just one irreducible representation, mS_2^-, reproduced the relative intensities of the magnetic diffraction peaks. In this discussion, we make reference to four symmetry-equivalent crystallographic sites, defined with respect to the *Cmcm* unit cell, which comprise the full cobalt sublattice: Co1: $[0, y, \frac{1}{4}]$; Co2: $[\frac{1}{2}, \frac{1}{2} - y, \frac{3}{4}]$; Co3: $[\frac{1}{2}, \frac{1}{2} + y, \frac{1}{4}]$; Co4: $[0, 1 - y, \frac{3}{4}]$, where $y = 0.1911(6)$ at 100 K.

Matrices of the two-dimensional irreducible representation mS_2^-, for selected symmetry generators of the parent space group *Cmcm*, are given in the top row of Table II. The magnetic order parameter can take one of three distinct directions in the space spanned by the irreducible representation: (η, η), $(\eta, 0)$, or (η, ϵ). In all cases, the

respective magnetic structures involve moments oriented strictly parallel to the orthorhombic c axis. As all of the Co ions in the lattice are structurally equivalent, and therefore have the same chemical environment, all of the moments on these ions are constrained to be equal in magnitude. The only order parameter direction consistent with this constraint is $(\eta, 0)$.

The order parameter $(\eta, 0)$ corresponds to a magnetic structure that lowers the symmetry of the system to monoclinic (magnetic space group P_a2_1/m[30]). Magnetic moments on the Co1, Co2 and Co4 sites are parallel, but with the moment on the Co3 sites aligned antiparallel. A second domain exists with order parameter $(0, \eta)$, in which Co1, Co3, and Co4 sites are aligned parallel to each other, with Co2 antiparallel. Inspection of the mS_2^- matrices given in Table II shows that the $(\eta, 0)$ and $(0, \eta)$ magnetic domains are interchanged by the symmetry operator $\{m_x|0,0,0\}$, which is indeed broken below the magnetic phase transition. Furthermore, the $(\eta, 0)$ and $(0, \eta)$ domains are described by single propagation vectors, $\mathbf{k}_1$ and $\mathbf{k}_2$, respectively, which are also related by m_x. The two domains are shown in Fig. 4, with the schematic in the right hand panes illustrating the two propagation vector directions. We note that the two domains are indistinguishable in our powder diffraction data. The magnitude of the Co moment was refined against the diffraction data and found to be $2.72(1)\,\mu_B$ at 1.5 K (see Fig. 3(b)). Its temperature dependence is shown in Fig. 2(d) and matches that found from μSR.

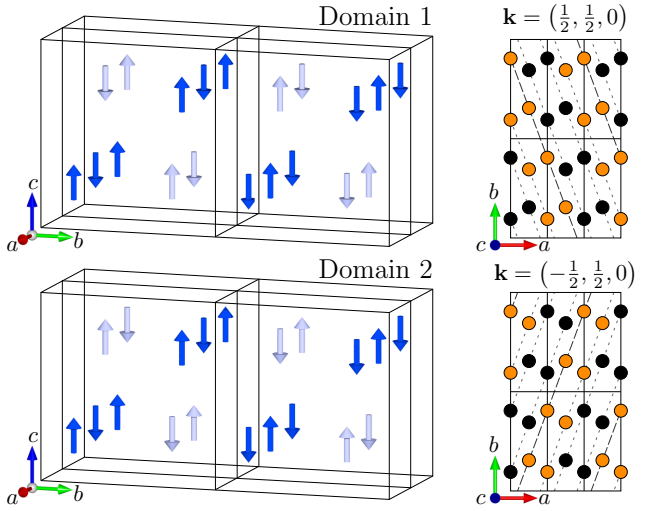

FIG. 4. The magnetic structure of $CoTi_2O_5$. In the left hand panels four $Cmcm$ unit cells are drawn, which represent a full repeating unit of the magnetic structure. Co1 and Co4 moments, drawn as dark blue arrows, are related to the Co2 and Co3 moments, drawn as light blue arrows, by C-centring. Note that the two domains related by the $\{m_x|0,0,0\}$ symmetry operator of the parent structure can be obtained by reversing the sign of the Co2 and Co3 moments. The diagrams on the right hand side illustrate the two propagation vectors associated with the two domains, where antiparallel moments are drawn as orange and black spheres. Planes of parallel moments are denoted by faint dotted grey lines, and the periodicity of the magnetic structure is highlighted by the bold dashed grey lines.

IV. DISCUSSION

A. Spin-Jahn-Teller effect

The only nearest neighbour, superexchange interactions between cobalt atoms (Co–O–Co) connect magnetic moments along the a-axis in Coi–Coi chains. All other nearest-neighbour interactions are mediated by super-superexchange (Co–O–O–Co). One can assume that the superexchange interactions are dominant and, by the experimentally determined magnetic structure, are antiferromagnetic. All exchange interactions between the (Co1,Co4) and (Co2,Co3) sites, coloured dark and light blue in Fig. 4 respectively, are exactly frustrated by the m_x symmetry element. This frustration will likely lead to one dimensional ordering of the a-axis chains above T_N, but below the mean field energy of the dominant superexchange interaction, consistent with the missing entropy evidenced in the heat capacity. For long range order to develop in $CoTi_2O_5$, the m_x mirror symmetry must be broken either at a structural phase transition above T_N, or through the spin Jahn-Teller effect, in which the primary magnetic order parameter couples to a secondary, symmetry breaking structural order parameter spontaneously at T_N.[2,3] In the absence of any experimental evidence for a higher T structural phase transition, we discuss possible magneto-structural coupling schemes.

The lowest order, free energy invariant that can couple the magnetic order to symmetry breaking crystallographic distortions must be quadratic in the magnetic moments (to be time-reversal even), and linear in the structural order parameter. On traversing the crystal in the direction of the propagation vector, magnetic moments change sign from one unit cell to the next. However, considering the square of the moments each unit cell is the same. Hence, the square of the order parameter components, η^2 and ϵ^2, must couple to a $\mathbf{k}_s = (0,0,0)$, Γ-point structural distortion if the coupling term is to be invariant by translation, as required. Through exhaustive searches performed using the ISOTROPY suite,[31,32] the only linear-quadratic invariant that can couple a non-trivial Γ-point structural distortion to the magnetic order is $\delta\left(\eta^2 - \epsilon^2\right)$, where the irreducible representation of the structural order parameter, δ, is Γ_2^+. For completeness, we should also consider the trivial coupling invariant $\xi\left(\eta^2 + \epsilon^2\right)$, where the structural order parameter ξ transforms according to the totally symmetric Γ_1^+ irreducible representation, i.e. structural distortions that were already allowed within the $Cmcm$ parent symmetry can also occur at T_N. The atomic displacements of Γ_1^+ and Γ_2^+ are tabulated in Table III and IV respectively (see Appendix B). High resolution laboratory based x-ray powder diffraction experiments yielded no evidence

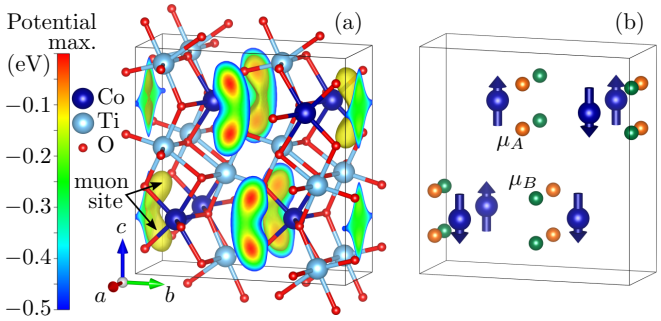

FIG. 5. (a) Electrostatic Coulomb potential of $CoTi_2O_5$ computed with DFT. The potential is shown on the surface of the unit cell up to 0.5 eV below its maximum value, and a yellow isosurface is plotted within the unit cell at 0.25 eV below the maximum. (b) Muon positions inside $CoTi_2O_5$, with the two symmetry inequivalent groups μ_A and μ_B marked in orange and green respectively. The spin structure of domain 1 is shown on the Co ions.

of these distortions below T_N. We therefore assume that any structural distortion in $CoTi_2O_5$ will be small, and the following calculations utilize the undistorted unit cell.

B. Density functional calculations

Density Functional Theory (DFT) calculations were carried out using the plane-wave program *Quantum Espresso*,[33] and utilized the generalized gradient approximation for the exchange-correlation functional.[34] The ions were modelled with ultrasoft pseudopotentials,[35] while a norm-conserving hydrogen pseudopotential was used to model the muon. The energy cutoffs for the wavefunction and the charge density were set to 60 Ry and 600 Ry, respectively, and the integration over the Brillouin zone was carried out using a $5 \times 3 \times 3$ Monkhorst-Pack k-space grid.[36] These parameters were found to yield well-converged results that predicted atomic positions and lattice parameters of the bulk material within 3% of the experimentally observed ones.[20] The electrostatic Coulomb potential was computed from the converged electron density.

In order to establish the potential muon stopping sites in $CoTi_2O_5$, we first employed DFT calculations to map out the electrostatic Coulomb potential of the refined crystal structure, plotting the results using the VESTA software[37] in Fig 5(a). The maxima of such a potential map are a reliable approximation to the muon sites as they correspond to low energies needed to add a positive charge, such as the muon.[38,39] By considering the electrostatic potential alone we identified a single muon site candidate with fractional coordinates of roughly $[0.45, 0.05, 0.15]$. Note that this site is only approximate as the electrostatic potential approach does not consider local distortions caused by the muon itself. We also carried out relaxation calculations which allow for such muon-induced distortions. These gave a single symmetry-inequivalent muon stopping site at the general position $[0.322, 0.03, 0.151]$ with a 1.0 Å O–H-like bond with the nearest oxygen. This is in line with the approximate position we identified from the electrostatic potential.

C. Dipolar fields

There are 16 symmetry equivalent muon sites in the $Cmcm$ parent structure, which are split into two groups of eight in the magnetic unit cell, related by the broken m_x symmetry, and are denoted by μ_A and μ_B in Fig. 5(b). The muon stopping probability is dependent upon the electrostatic potential local to the stopping sites, and under a small structural distortion induced at the phase transition, μ_A and μ_B become structurally inequivalent, and therefore result in different muon stopping probabilities. Changing from one magnetoelastic domain to another swaps the stopping probabilities of the two subgroups. The symmetry of the magnetic structure also dictates that μ_A and μ_B will have different local magnetic fields. Using the muon stopping site and magnetic structure determined above, we calculated the expected dipolar field at the muon site resulting from the Co ions. The dipolar field from moments $\mathbf{m}_i$ and positions $\mathbf{r}_i$ can be found via

$$\mathbf{B}_{\text{dip}} = \frac{\mu_0}{4\pi} \sum_i \frac{3\,(\mathbf{m_i} \cdot \hat{\mathbf{r}}_{i\mu})\,\hat{\mathbf{r}}_{i\mu} - \mathbf{m_i}}{|\mathbf{r}_{i\mu}|^3}, \qquad (2)$$

where $\hat{\mathbf{r}}_{i\mu}$ is the normalized vector between the muon and the moment $\mathbf{m}_i$. We therefore calculate the dipolar fields at the two sites to be 335(1) mT and 277(1) mT, in excellent agreement with our experimental observations at low T. As the area under the higher-field peak in Fig. 1(d) is larger than that of the lower-field peak, this suggests that the muon site experiencing this field is preferentially occupied. By comparing the energies at the muon sites under small distortions, we present a possible coupling between a shear distortion and the magnetic domains in Appendix C that could explain this.

Finally we consider the additional feature marked by an asterisk in Fig. 1(d) at ≈ 400 mT. This feature likely arises due to a Co ion occupying the nearest Ti site so that a small fraction of muons stopping close to this defect experience a slightly larger field. Indeed, modelling this disorder gives a field at the muon site of ≈ 410 mT, consistent with the experimental value.

V. CONCLUSION

To conclude, we have identified long range magnetic order in $CoTi_2O_5$, which is antiferromagnetic with $\mathbf{k} = (\pm\frac{1}{2}, \frac{1}{2}, 0)$. Frustration in the super-superexchange interactions, along with the absence of a structural distortion above $T_N \approx 26$ K, indicate that the magnetic transition

must be coupled to a structural transition at T_N in order to relieve the frustration. This coupling occurs due to the spin Jahn-Teller effect, which has so far only been identified in higher-symmetry crystal structures.[2–5] Our results show that magnetic order driven by spin-phonon coupling can be extended to lower-symmetry systems. While the predicted distortion in $CoTi_2O_5$ was not resolvable in high resolution laboratory based x-ray powder diffraction experiments, it may be possible to resolve using higher-resolution synchrotron x-ray powder diffraction experiments. The study of compounds structurally related to $CoTi_2O_5$ may provide further insight into the conditions required for the spin Jahn-Teller effect to, or not to, occur.

ACKNOWLEDGMENTS

F.K.K.K. thanks Lincoln College, Oxford, for a doctoral studentship. R.D.J. acknowledges support from a Royal Society University Research Fellowship. This work is supported by EPSRC (UK) grants EP/N023803/1 and EP/N024028/1. Part of this work was performed at the Science and Technology Facilities Council (STFC) ISIS Facility, Rutherford Appleton Laboratory, and part at SμS, the Swiss Muon Source (PSI, Switzerland). The authors would like to acknowledge the use of the University of Oxford Advanced Research Computing (ARC) facility in carrying out this work.[40]

Appendix A: Time-domain μSR fitting

In Section III B we discussed the fitting of the muon data in the frequency domain. It is also possible to fit the data in the time domain and the conclusions are the same. The data plotted in Fig. 1(a) (and also in Fig. 6(a), to illustrate the absolute size of the signals) can be fitted for $T < T_N$ in the time domain using a sum of two oscillating components with a Lorentzian relaxation, and a background term:

$$A(t) = A_r \left(a_1 \cos\left(\gamma_\mu B_1 t\right) e^{-\lambda_1 t} + a_2 \cos\left(\gamma_\mu B_2 t\right) e^{-\lambda_2 t}\right) + A_b, \quad \text{(A1)}$$

where $\gamma_\mu = 2\pi \times 135.5\,\mathrm{MHzT}^{-1}$ is the gyromagnetic ratio of the muon. The first two terms correspond to muons precessing in the internal fields of the sample, as described in Section III B. The relative amplitudes of these two components were fixed to their low temperature values ($a_1 \approx 0.37$; $a_1 + a_2 = 1$). The third term is a background term ($A_b \approx 5\%$) and contains contributions from the non-precessing part of the previous two components (corresponding to the projection of the local field on to the initial muon polarisation direction) as well as a small contribution from muons which land in the cryostat and sample holder. These experiments were performed with the muon polarization at $\sim 45°$ to the muon momentum (to maximise the chance of observing a precession signal) and so quantitative analysis of the amplitudes should be deferred to a future study of directional dependence using a conventional zero field μSR geometry. The fitted values of the internal fields B_i and relaxation rates λ_i are shown in Figs. 6(b) and (c) respectively; the values extracted from time-domain fitting are consistent with those from the field-domain fitting (presented in Section III B).

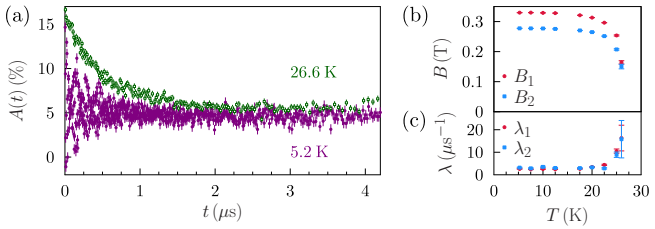

FIG. 6. (a) Raw μSR data at two selected temperatures. These data were recorded with the muon spin at 45° to the muon momentum, leading to a reduced total asymmetry. The temperature dependences of (b) the local fields and (c) relaxation rates.

In order to extract T_N and the internal field at the muon site at $T = 0$, we can use a relationship $B = B_0\left(1 - (T/T_N)^\alpha\right)^\beta$, also used for fitting the temperature dependence of the Co moment extracted from PND. While B_0 for both muon sites and T_N were presented in Section III B, we also find $\alpha \approx 4$–6 and $\beta \approx 0.1$–0.2 for the muon and neutron data sets. Note that this relationship is phenomenological and these parameters should not be over-interpreted. The low values of β are consistent with a precipitous drop in moment as the transition is approached from below.

Appendix B: Structural order parameter and free energy invariants

As discussed in Section III D, the lowest order free energy invariant that couples the two dimensional magnetic order parameter, (η, ϵ), to symmetry breaking structural distortions with order parameter δ is written as

$$\delta\left(\eta^2 - \epsilon^2\right). \quad \text{(B1)}$$

The magnetic order, (η, ϵ), and the structural order, δ, transform according to the irreducible representations mS_2^- and Γ_2^+ respectively. Matrix representations of mS_2^- and Γ_2^+ for selected symmetry generators are given in Table II. One can see that the above invariant is consistent with these matrices. For example, the structural distortion must be symmetric in $\{m_z|0,0,\frac{1}{2}\}$ and $\{1|0,0,0\}$, and antisymmetric in $\{m_x|0,0,0\}$ upon switching between $(\eta, 0)$ and $(0, \eta)$ magnetic domains. The pattern of atomic displacements that transform according to Γ_2^+ are listed in Table III.

There is also the trivial coupling invariant

$$\xi\left(\eta^2 + \epsilon^2\right), \quad \text{(B2)}$$

Irrep.	$\{m_z\|0,0,\frac{1}{2}\}$	$\{m_x\|0,0,0\}$	$\{\bar{1}\|0,0,0\}$	$\{1\|1,0,0\}$	$\{1\|0,1,0\}$	T
[1.pt] mS_2^-	$\begin{bmatrix}1 & 0\\ 0 & 1\end{bmatrix}$	$\begin{bmatrix}0 & -1\\ -1 & 0\end{bmatrix}$	$\begin{bmatrix}-1 & 0\\ 0 & -1\end{bmatrix}$	$\begin{bmatrix}-1 & 0\\ 0 & -1\end{bmatrix}$	$\begin{bmatrix}-1 & 0\\ 0 & -1\end{bmatrix}$	$\begin{bmatrix}-1 & 0\\ 0 & -1\end{bmatrix}$
Γ_1^+	1	1	1	1	1	1
Γ_2^+	1	−1	1	1	1	1

TABLE II. Irreducible representation matrices for selected symmetry generators of space group $Cmcm$, calculated using the ISOTROPY suite.[31,32] T is the time reversal operator, m denotes magnetic representations, and the S point is associated with propagation vectors $\left(\pm\frac{1}{2},\frac{1}{2},0\right)$ in accordance with the notation of Miller and Love.[41]

where the structural order parameter ξ transforms according to the totally symmetric Γ_1^+ irreducible representation, i.e. structural distortions that were already allowed within the $Cmcm$ parent symmetry can also occur at T_N. The pattern of atomic displacements that transform according to Γ_1^+ are listed in Table IV.

Atom	x_{sg}	y_{sg}	z_{sg}	dx	dy	dz
Co, O1	y	1/4	$2y$	−1	0	0
	$-y$	3/4	$-2y$	1	0	0
Ti, O2, O3	y	z	$2y$	−1	0	0
	$-y$	$-z$	$-2y$	1	0	0
	y	$-z+\frac{1}{2}$	$2y$	−1	0	0
	$-y$	$z+\frac{1}{2}$	$-2y$	1	0	0

TABLE III. The pattern of atomic displacements, strains, and shears that transform according to Γ_2^+. They are represented by the order parameter δ and predicted to occur to some extent at T_N. The space group is $P2_1/m$, the basis with respect to the parent is $\{(-1,0,0),(0,0,1),(\frac{1}{2},\frac{1}{2},0)\}$, and the origin shift is $(0,0,0)$. There is no strain, and the shear is a monoclinic shear distortion of the orthorhombic lattice, with the $Cmcm$ c-axis unique.

Appendix C: Structural distortions

The distortion discussed above causes a monoclinic shear in the unit cell with the c-axis unique, or a series of atomic displacements. This manifests in a perturbation of γ, the angle between the a and b directions. This perturbation can either result in an increase or decrease of γ, dependent on the domain. In the absence of the monoclinic distortion, $\gamma = 90°$ and both muon sites are structurally equivalent (although they are magnetically inequivalent). If $\gamma \neq 90°$, the two sites μ_A and μ_B become structurally inequivalent, and their ground state energies differ. The difference between the ground state energies $\Delta E_{AB} = E_{\mu_A} - E_{\mu_B}$, where E_{μ_i} is the ground state energy of the unit cell containing a muon in site μ_i, is plotted in Fig. 7. When $\Delta E_{AB} < 0$, muons preferably occupy μ_A, whereas if $\Delta E_{AB} > 0$, muons preferably occupy μ_B. In our μSR data a higher fraction of muons appear to thermalize at the higher-field sites. By simulating the local dipolar field at the muon site for $\gamma \neq 0$, we find a possible correspondence between γ and the domain, shown in Fig. 7(b). In this configuration, the high-field site is always energetically favorable.

Atom	x_{sg}	y_{sg}	z_{sg}	dx	dy	dz
Co, O1	y	$\frac{1}{4}$	$2y$	$\frac{1}{2}$	0	1
	$-y$	$\frac{3}{4}$	$-2y$	$-\frac{1}{2}$	0	−1
Ti, O2, O3	y	z	$2y$	$\frac{1}{2}$	0	1
	$-y$	$-z$	$-2y$	$-\frac{1}{2}$	0	−1
	y	$-z+\frac{1}{2}$	$2y$	$\frac{1}{2}$	0	1
	$-y$	$z+\frac{1}{2}$	$-2y$	$-\frac{1}{2}$	0	−1
	y	z	$2y$	0	1	0
	$-y$	$-z$	$-2y$	0	−1	0
	y	$-z+\frac{1}{2}$	$2y$	0	−1	0
	$-y$	$z+\frac{1}{2}$	$-2y$	0	1	0

TABLE IV. The pattern of atomic displacements, strains, and shears that transform according to Γ_1^+. They are represented by the order parameter ξ and predicted to occur to some extent at T_N. The space group is $P2_1/m$, the basis with respect to the parent is $\{(-1,0,0),(0,0,1),(\frac{1}{2},\frac{1}{2},0)\}$, and the origin shift is $(0,0,0)$. There are three independent components of uniaxial strain parallel to the $Cmcm$ unit cell axes, and no shear.

* franziska.kirschner@physics.ox.ac.uk
† stephen.blundell@physics.ox.ac.uk

[1] G. A. Gehring and K. A. Gehring, Rep. Prog. Phys. **38**, 1 (1975).
[2] Y. Yamashita and K. Ueda, Phys. Rev. Lett. **85**, 4960 (2000).
[3] O. Tchernyshyov, R. Moessner, and S. L. Sondhi, Phys. Rev. Lett. **88**, 067203 (2002).
[4] M. Onoda and J. Hasegawa, J. Phys. Condens. Matter **15**, L95 (2003).
[5] T. Watanabe, S. I. Ishikawa, H. Suzuki, Y. Kousaka, and K. Tomiyasu, Phys. Rev. B **86**, 144413 (2012).

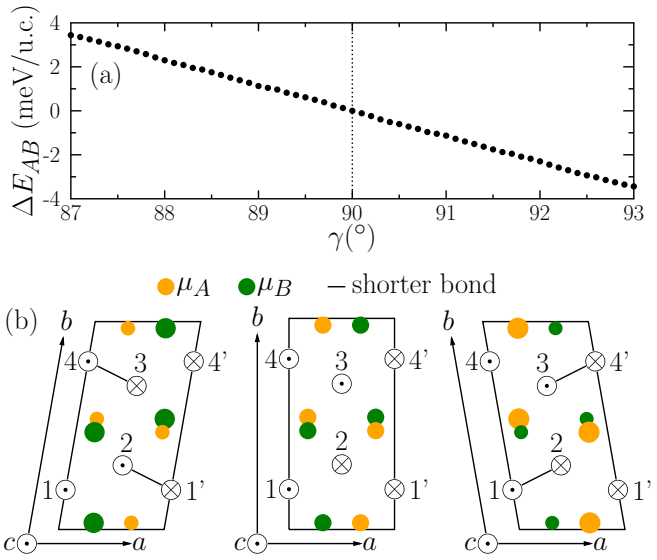

FIG. 7. (a) The γ dependence of the difference in energy between the two structurally inequivalent sites $\Delta E_{AB} = E_{\mu_A} - E_{\mu_B}$. E_{μ_i} is the DFT-calculated energy of the relaxed unit cell with the μ_i site occupied by a muon. (b) shows the domain structure at shearing angles above and below $\gamma = 90°$ as predicted by the μSR data in Section III B. The muon sites μ_i are also plotted, where the larger circles indicate muon sites that are energetically favourable.

[6] O. Waldmann, C. Dobe, S. T. Ochsenbein, H. U. Güdel, and I. Sheikin, Phys. Rev. Lett. **96**, 027206 (2006).
[7] O. Waldmann, Phys. Rev. B **75**, 174440 (2007).
[8] S. Ogawa and S. Waki, J. Phys. Soc. Jpn. **20**, 540 (1965).
[9] J. K. Srivastava, S. Ramakrishnan, V. R. Marathe, G. Chandra, R. Vijayaraghava, J. A. Kulkarni, V. S. Darshane, and S. Singh, J. Phys. C **20**, 2139 (1987).
[10] G. Gavoille, J. Hubsch, and S. Koutani, J. Magn. Magn. Mater. **102**, 283 (1991).
[11] S. Nayak, S. Thota, D. C. Joshi, M. Krautz, A. Waske, A. Behler, J. Eckert, T. Sarkar, M. S. Andersson, R. Mathieu, V. Narang, and M. S. Seehra, Phys. Rev. B **92**, 214434 (2015).
[12] D.-C. Kim and S.-K. Ihm, Environ. Sci. Technol. **35**, 222 (2001).
[13] J. Zhu and Q. Gao, Microporous and Mesoporous Mater. **124**, 144 (2009).
[14] V. G. Harris, A. Geiler, Y. Chen, S. D. Yoon, M. Wu, A. Yang, Z. Chen, P. He, P. V. Parimi, X. Zuo, C. E. Patton, M. Abe, O. Acher, and C. Vittoria, J. Magn. Magn. Mater. **321**, 2035 (2009).
[15] C. P. Sandhya, B. John, and C. Gouri, Ionics **20**, 601 (2014).
[16] R. Ye, H. Fang, Y.-Z. Zheng, N. Li, Y. Wang, and X. Tao, ACS Appl. Mater. Interfaces **8**, 13879 (2016).
[17] X. Chu, X. Liu, G. Wang, and G. Meng, Mater. Res. Bull. **34**, 1789 (1999).
[18] T. S. Chao, W. M. Ku, H. C. Lin, D. Landheer, Y. Y. Wang, and Y. Mori, IEEE Trans. Electron Devices **51**, 2200 (2004).
[19] B. Brezny and A. Muan, J. Inorg. Nucl. Chem. **31**, 649 (1969).
[20] H. Müller-Buschbaum and M. Waburg, Monatsh Chem. **114**, 21 (1983).
[21] A. Navrotsky, Am. Mineral. **60**, 249 (1975).
[22] A. Yankin, O. Vikhreva, and V. Balakirev, J. Phys. Chem. Solids **60**, 139 (1999).
[23] K. T. Jacob and G. Rajitha, J. Chem. Thermodyn. **42**, 879 (2010).
[24] A. M. Balbashov, A. A. Mukhin, V. Y. Ivanov, L. D. Iskhakova, and M. E. Voronchikhina, Low Temp. Phys **43**, 965 (2017).
[25] L. C. Chapon, P. Manuel, P. G. Radaelli, C. Benson, L. Perrott, S. Ansell, N. J. Rhodes, D. Raspino, D. Duxbury, E. Spill, and J. Norris, Neutron News **22**, 22 (2011).
[26] J. Rodríguez-Carvajal, Physica B **192**, 55 (1993).
[27] S. J. Blundell, Contemp. Phys. **40**, 175 (1999).
[28] A. A. Yaouanc and P. D. de. Réotier, *Muon spin rotation, relaxation, and resonance : applications to condensed matter* (Oxford University Press, 2011) p. 486.
[29] F. L. Pratt, Physica B **710**, 289 (2000).
[30] The P_a2_1/m magnetic unit cell has a $\{[-2,0,0],[0,0,1],[\frac{1}{2},\frac{1}{2},0]\}$ change of basis with respect to the *Cmcm* parent structure, plus an origin shift of $[-\frac{1}{4},\frac{1}{4},0]$. N.B. The orthorhombic *Cmcm* *c*-axis is parallel to the P_a2_1/m *b*-axis in the standard setting.
[31] B. J. Campbell, H. T. Stokes, D. E. Tanner, and D. M. Hatch, J. Appl. Crystallogr. **39**, 607 (2006).
[32] H. T. Stokes, D. M. Hatch, and B. J. Campbell, *ISOTROPY Software Suite* (2007).
[33] P. Gianozzi *et al.*, J. Phys. Condens. Matter **21**, 395502 (2009).
[34] J. P. Perdew, K. Burke, and M. Ernzerhof, Phys. Rev. Lett. **77**, 3865 (1996).
[35] A. M. Rappe, K. M. Rabe, E. Kaxiras, and J. D. Joannopoulos, Phys. Rev. B **41**, 1227 (1990).
[36] H. J. Monkhorst and J. D. Pack, Phys. Rev. B **13**, 5188 (1976).
[37] K. Momma and F. Izumi, J. Appl. Crystallogr. **41**, 653 (2008).
[38] J. S. Möller, P. Bonfà, D. Ceresoli, F. Bernardini, S. J. Blundell, T. Lancaster, R. De Renzi, N. Marzari, I. Watanabe, S. Sulaiman, and M. I. Mohamed-Ibrahim, Phys. Scripta **6**, 068510 (2013).
[39] F. R. Foronda, F. Lang, J. S. Möller, T. Lancaster, A. T. Boothroyd, F. L. Pratt, S. R. Giblin, D. Prabhakaran, and S. J. Blundell, Phys. Rev. Lett. **114**, 017602 (2015).
[40] A. Richards, *https://doi.org/10.5281/zenodo.22558* (2015).
[41] S. Miller and W. F. Love, *Tables of irreducible representations of space groups and co-representations of magnetic space groups* (Pruett Press, Boulder, Colorado, 1967).